Cell Reports
Physical Science

CellPress
OPEN ACCESS

Article

High-current water electrolysis performance of metal phosphides grafted on porous 3D N-doped graphene prepared without using phosphine

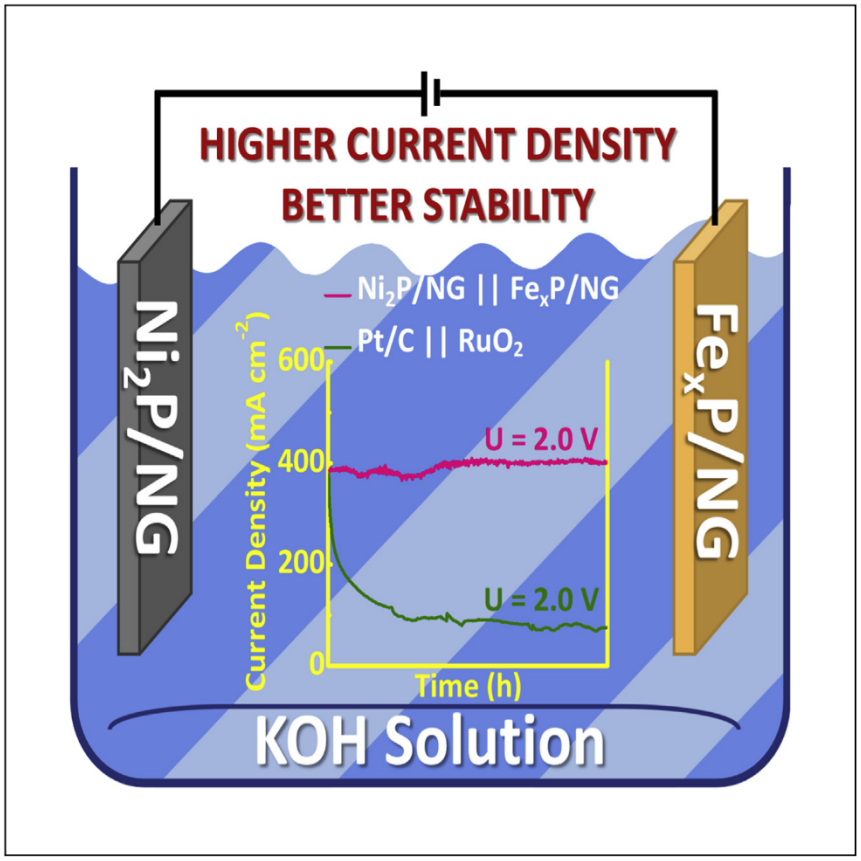

Transition metal phosphides are promising catalysts for water electrolysis but are commonly prepared using hazardous phosphines. Here Hu et al. prepare electrodes consisting of metal phosphide nanoparticles supported on porous 3D graphene, avoiding the use of hazardous precursors, catalyzing water electrolysis at high current density near industrial requirements.

Jiajun Hu, Lu Peng, Ana Primo, Josep Albero, Hermenegildo García

joalsan6@upvnet.upv.es (J.A.)
hgarcia@qim.upv.es (H.G.)

Highlights

Synthetic procedure for preparing metal phosphides avoiding the use of toxic reagents

The method creates a strong interaction between metal phosphides and the support

Ni_2P and Fe_xP on N-doped graphene electrodes have been prepared for water electrolysis

These can operate at 400 mA/cm^2 for 50 h

Hu et al., Cell Reports Physical Science 3, 100873
May 18, 2022
https://doi.org/10.1016/j.xcrp.2022.100873

Cell Reports
Physical Science

CellPress
OPEN ACCESS

Article

High-current water electrolysis performance of metal phosphides grafted on porous 3D N-doped graphene prepared without using phosphine

Jiajun Hu,[1] Lu Peng,[1] Ana Primo,[1] Josep Albero,[1,*] and Hermenegildo García[1,*]

SUMMARY

Development of efficient and stable electrodes for hydrogen and oxygen evolution from water constituted of abundant elements and prepared by sustainable and scalable procedures is of considerable importance for producing green hydrogen from renewable electricity. Herein, a method for the preparation of Ni_2P, Fe_2P, and FeP supported on N-doped graphene (NiP/NG and FeP/NG) is reported. The procedure uses metal salts, phosphorous oxide, and chitosan as precursors of metal phosphide and N-doped graphene, avoiding the use of undesirable and hazardous precursors, such as PH_3 or NaH_2PO_2, and rendering a material with a strong metal phosphide-graphene interaction. Moreover, NiP/NG and FeP/NG electrodes are demonstrated to be more efficient than the benchmark catalysts Pt/C and RuO_2, for hydrogen evolution reaction and oxygen evolution reaction, respectively, at a large current density (300 mA/cm^2). In addition, water electrolysis was carried out using NiP/NG//FeP/NG electrodes, also demonstrating improved efficiency and stability compared with Pt/C//RuO_2 at a current density (400 mA/cm^2) near industrial requirements.

INTRODUCTION

Hydrogen is considered a clean energy vector and reagent that can be used either as intermediate for the production of highly valuable chemicals (NH_3, MeOH, or polymers, among others) or directly as fuel.[1] In the latter case, H_2 can be used in fuel cells, where H_2 oxidation and O_2 reduction reactions take place to convert chemical energy into electricity.[2] Nowadays, most of the H_2 produced for industrial applications is obtained from steam reforming of methane and hydrocarbons,[3] which is considered an energy intensive process, and it generates CO_2 emissions, causing severe environmental concerns. Hence, sustainable and environmentally friendly mass production of high purity H_2 is considered a great challenge to mitigate both the energy crisis and climate change.

Water electrolysis using green electricity from renewable sources (photovoltaics, wind turbines, etc.), appears to be a viable approach for large-scale production of high-purity H_2.[4,5] Water electrolysis consists of two half-reactions, the hydrogen evolution reaction (HER) and the oxygen evolution reaction (OER), following Equations 1 and 2, respectively. Nowadays, commercially available electrodes for both HER and OER are based on scarce and high-priced critical raw materials such as Pt for HER and IrO_2 or RuO_2 for OER, among others.[6] Moreover, typical commercial electrolyzers work at current densities between 200 and 500 mA/cm^2 at approximately 2 V, in alkali media.[7] Hence, the design of high-efficiency, cost-effective,

[1]Instituto Universitario de Tecnología Química CSIC-UPV, Universitat Politècnica de València-Consejo Superior de Investigaciones Científicas, Universitat Politecnica de Valencia, Avda. de los Naranjos s/n, 46022 Valencia, Spain

*Correspondence:
joalsan6@upvnet.upv.es (J.A.),
hgarcia@qim.upv.es (H.G.)

https://doi.org/10.1016/j.xcrp.2022.100873

and robust electrocatalysts based on abundant and low-cost materials for overall water splitting is of paramount importance to minimize the costs of mass production of high-purity H_2 for industry.

$$2H^+ + 2e^- \rightarrow H_2 \quad \text{(Equation 1)}$$

$$2H_2O \rightarrow O_2 + 4H^+ + 4e^- \quad \text{(Equation 2)}$$

In this regard, earth-abundant, non-noble-metal-based electrocatalysts, such as metal oxides, carbides, nitrides, chalcogenides, phosphates, and phosphides, have been widely investigated in recent years.[8–10] Among them, transition metal phosphides have attracted growing interest as catalysts for water splitting due to their low overpotential, high electrical conductivity, optimum catalytic activity, and chemical stability.[11] However, metal phosphides have been typically prepared by phosphidation of metal oxides using extremely poisonous, hazardous, and explosive phosphine. To facilitate the process, beside the direct use of PH_3, this poisonous gas can be generated *in situ* by reduction of hypophosphite (NaH_2PO_2) or from alkyl phosphines (trioctylphosphine, triphenylphosphine, etc.).[12] To circumvent the use or generation of PH_3, alternative synthetic procedures, such as the direct reaction between transition metals and elemental phosphorous, in both gas and liquid phase, plasma treatment or electrodeposition of precursors have been also reported for metal phosphide preparation.[13,14] However, some of these alternative methods require high vacuum and expensive equipment and/or present low purity, forming metal phosphates/phosphides mixtures. For those reasons, these methods are not suitable for large-scale production of pure metal phosphides.

Herein we present an easy preparation method of high-purity crystalline metal phosphides that avoids the use or generation of hazardous species during synthesis. Specifically, FeP/Fe_2P and Ni_2P nanoparticles supported on porous 3D N-doped graphene (FeP/NG and NiP/NG) have been prepared and their performance as electrocatalysts for HER and OER evaluated. Graphene-based materials have been widely employed as electrocatalysts support in the last years.[15] The combination of totally accessible high surface area, strong adsorption capacity, high electrical conductivity, and the possibility to generate defects acting as catalytic sites, together with sustainability when obtained from biomass wastes justify the interest of graphene and derivatives as electrocatalysts.[16] In addition, graphenes can act also as supports of metallic compounds, and depending on the preparation conditions, they can establish a strong interaction with the supported particle that can serve to tune the electronic density at the interphase and stabilize the particles under operation conditions.

The use of metal phosphides supported on graphene derivatives has been widely investigated recently, obtaining very promising overpotentials for HER and OER.[17–19] However, most of these materials have been prepared using hazardous reagents. Moreover, due to their lack of stability, they are typically tested at current densities in the order of tens of mA/cm^2, still far from their implementation in commercial applications that require current densities over 100 mA/cm^2.

Herein, NiP/NG and FeP/NG have been prepared following a sustainable and environmentally friendly method that use biomass wastes as source of NG and phosphate to form the metal phosphides. Besides, it has demonstrated low overpotentials for HER at high current densities of relevance for industrial uses. Similarly, FeP/NG exhibits a notable OER performance, with low overpotentials for high current densities. Remarkably, a two-electrode cell using FeP/NG and NiP/NG as anode

and cathode, respectively, displayed an impressive water splitting current density of 100 and 400 mA/cm^2 at 1.85 and 2 V, respectively, in alkali conditions for continuous 150 h test. In comparison, electrodes containing the commercial Pt/C and RuO_2 catalysts exhibited lower performance and stability at these high current densities. Benefiting from the easy, low-cost, and convenient scale-up of the preparation method, together with the low overpotentials for HER and OER and high stability at high current densities, the as-prepared FeP/NG and NiP/NG catalysts are promising candidates for its commercial implementation as electrocatalysts for overall water splitting.

RESULTS

Material synthesis and characterization

Fe and Ni phosphides supported on porous 3D graphene were synthetized following a simple and scalable preparation procedure. In brief, aqueous chitosan solutions containing adequate amounts of Fe^{2+} or Ni^{2+} salts were prepared. Chitosan is well known to adsorb high proportions of metal ions from water by complexation of the metal ions by amino groups of this polysaccharide.[20] The metal-chitosan solutions were subsequently precipitated in a 2 M NaOH solution, immediately forming hydrogel microspheres. The obtained metal-chitosan microspheres were washed with ethanol/water mixtures containing increasing ethanol content up to 100% ethanol. Then, the microspheres were impregnated with a P_4O_{10} solution in ethanol and dried in supercritical CO_2. The use of supercritical CO_2 drying has been previously reported[21] as a way to obtain highly porous and high-surface chitosan beds. Upon pyrolysis, the large surface area and porosity of the chitosan precursor is typically inherited by the resulting graphitic carbon matrix. High-resolution field effect scanning electron microscopy (HRFESEM) images of the microstructure of the obtained microspheres are shown in Figure S1 in the supplementary information. Finally, the resulting microspheres were pyrolyzed under Ar flow at 900°C for 2 h and the obtained samples denoted as FeP/NG and NiP/NG. For comparison purposes, the N-doped graphitic carbon support in the absence of metal phosphides (NG) was also prepared using the same procedure. This control in the absence of metal salts confirmed the formation of N-doped graphitic carbon matrix with a loose stacking of the defective graphene layers as previously reported.[21] Scheme 1 summarizes the preparation procedure.

The chemical composition of FeP/NG, NiP/NG, and NG samples was determined by inductively coupled plasma-optical emission spectroscopy (ICP-OES) and combustion elemental analysis, and the results are summarized in Table 1. From these data, we have estimated a metal phosphide content (wt %) in FeP/NG and NiP/NG samples of 35 and 39.2 wt %, respectively. Based on the ICP-OES results, empirical formulas of $Fe_{1.5}P$ and Ni_2P were obtained for FeP/NG and NiP/NG samples, respectively. The obtained $Fe_{1.5}P$ stoichiometry could be due to the presence of mixtures of Fe_2P and FeP.

It is worth noticing that the metal phosphides growth is accompanied by an N content (wt %) decrease from 8.1 in NG to 4.1 and 3.0 wt % in FeP/NG and NiP/NG, respectively. This reduction in N content can be ascribed to the catalytic activity of the metal nanoparticles during the formation of the graphene layers, as previously reported.[22]

The crystal structures of FeP/NG and NiP/NG were determined by X-ray diffraction (XRD). Figure S2A in the supplementary information shows very sharp, intense XRD

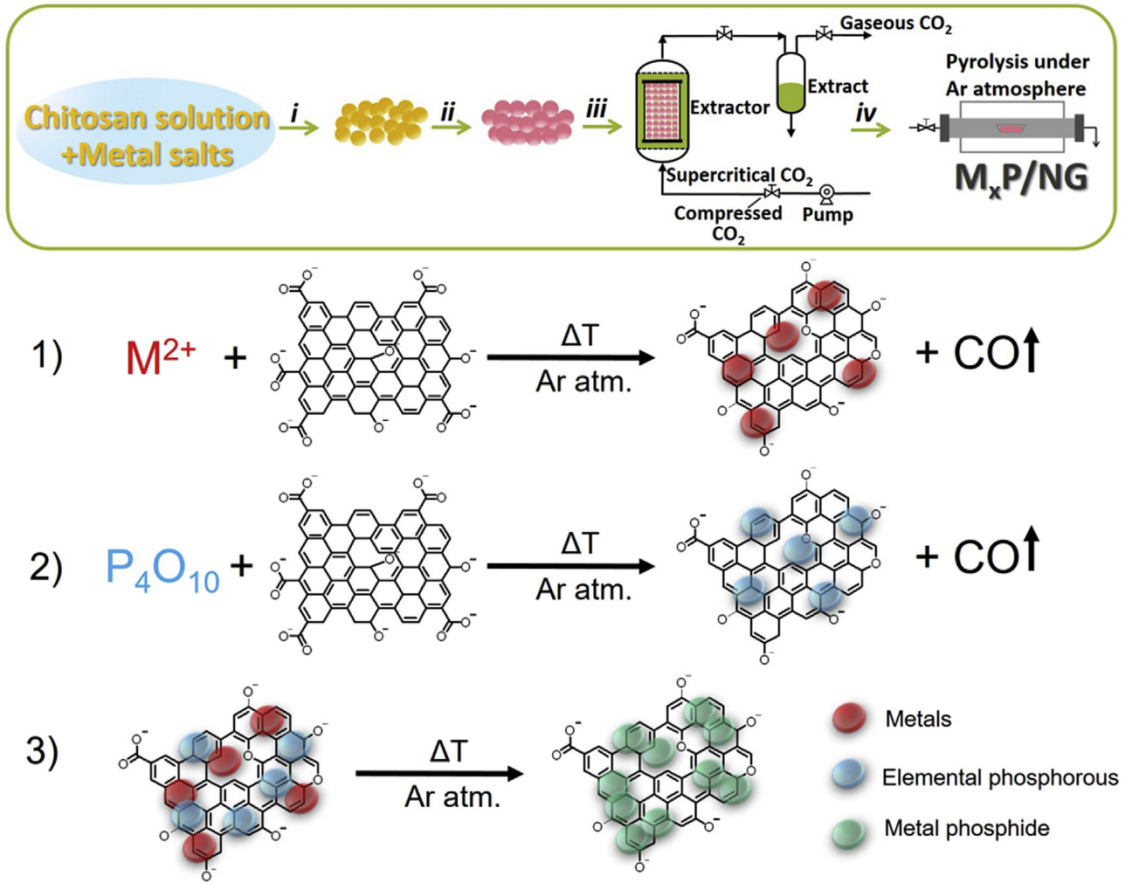

Scheme 1. Metal phosphides supported on 3D graphitic carbon preparation procedure and the proposed metal phosphide formation mechanism
Top: (i) chitosan-metal complexes precipitation and hydrogel microspheres formation, (ii) P_4O_{10} microspheres impregnation, (iii) supercritical CO_2 drying, and (iv) pyrolysis under Ar atmosphere. Bottom: proposed formation mechanism of the metal phosphides supported on N-doped graphitic carbons.

peaks for FeP/NG and NiP/NG, indicating the presence of crystalline structures in both samples. FeP/NG XRD pattern reveals the co-existence of Fe_2P (PDF-# NO.85-1725) and FeP (PDF-# NO.78-1443), in good agreement with the compositions anticipated by ICP-OES results. Meanwhile, the XRD pattern of NiP/NG shows only Ni_2P crystalline composition (PDF-# NO.03-0953). It is worth noticing that diffraction peaks corresponding to Fe or Ni oxides, carbides, or nitrides were undetectable in the diffractograms. All samples present also a broad and low intensity peak at 26.5°, attributed to π-π layer stacking in graphitic carbon matrix. As it will be commented subsequently, the electrocatalytic activity attributed to FeP/NG and NiP/NG is based on the coincidence of the XRD patterns with the reported patterns, with the precursors of the synthesis (metal acetates and phosphorous oxide) not playing any role.

Table 1. Chemical composition, specific surface area, and total pore volume of FeP/NG, NiP/NG, and NG samples

Sample	Metal (wt %)	P (wt %)	M + P (wt %)	C (wt %)	N (wt %)	S_{BET} (m^2/g)	V_{Pore} (m^3/g)
FeP/NG	25.7	9.3	35.0	39.8	4.1	249	1.01
NiP/NG	31.1	8.1	39.2	36.2	3.0	401	1.04
NG	–	–	–	79.5	8.1	272	0.66

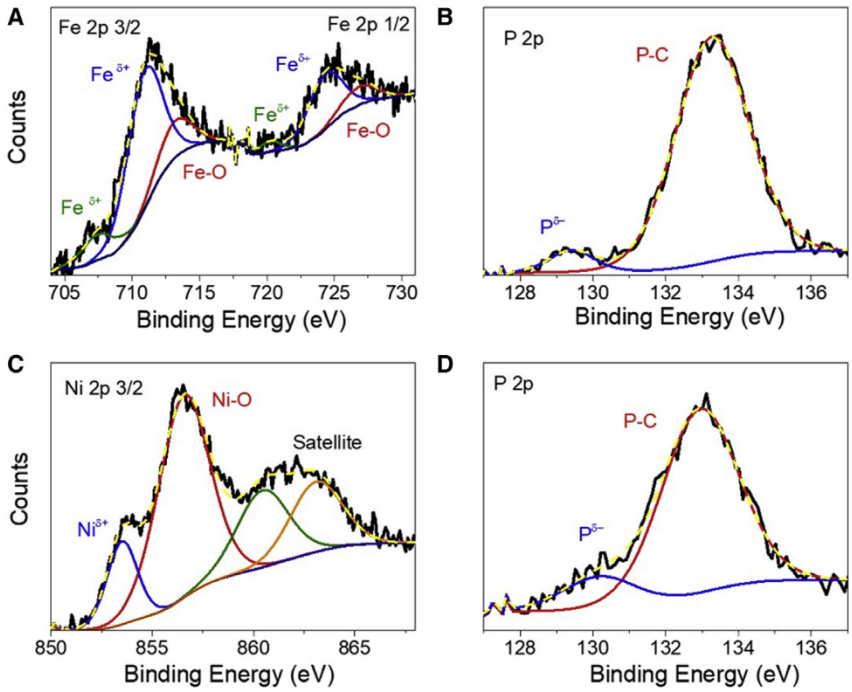

Figure 1. XPS analysis of FeP/NG and NiP/NG samples

XPS spectra of (A) Fe 2p, (B) P 2p in FeP/NG, and (C) Ni 2p3/2 and P 2p in NiP/NG.

Raman spectroscopy revealed the typical 2D (2,700 cm^{-1}), G (1,580 cm^{-1}), and D (1,350 cm^{-1}) bands characteristic to defective graphene obtained from the pyrolysis of chitosan in all samples, while no obvious vibration bands for Fe or Ni oxides, carbides, or nitrides were observed in the low-frequency region, in good agreement with the XRD results (see Figure S2B).[23]

The surface chemical analysis of FeP/NG and NiP/NG was investigated by X-ray photoelectron spectroscopy (XPS). High-resolution XPS peaks of Fe 2p, Ni 2p, and P 2p and their corresponding best deconvolution to their different components are presented in Figure 1. The Fe 2p spectrum of FeP/NG clearly exhibits two spin-orbit peaks (2p3/2 and 2p1/2). In these, the coupled components at 707.8/720.4 eV and 713.6/727.1 eV have been attributed to 2p3/2 and 2p1/2 of $Fe^{\delta+}$ (Fe in FeP) and oxidized Fe species of $FePO_4$, respectively.[24,25] This observation falls in contradiction with XRD and Raman results. However, it is worth noticing that while XRD probes the whole sample, XPS only provides information of the outermost layers, which are more prone to undergo spontaneous oxidation upon air and moisture exposure.[26] Moreover, there is an additional doublet at 711.1/724.7 eV assigned to $Fe^{\delta+}$ in Fe_2P. It is worth noticing that the component assigned to $Fe^{\delta+}$ in Fe_2P is +0.8 eV shifted from typical reported values.[27] This shift is attributed to electron density transfer to the graphenic support, demonstrating the strong interaction between the Fe_2P and graphene. The P 2p spectrum shows two peaks, the first centered at 129.3 eV assigned to P 2p3/2 and P 2p1/2 of low-valence $P^{\delta-}$, indicating Fe-P bonds. The second peak at 133.3 eV has been assigned to P-C bonds, while P-O signals should be located at 134.5 eV, as previously reported.[28] This is suggesting, on one hand, a strong interaction between the obtained phosphides and the N-doped graphitic support and, on the other hand, that the formation of PO_4 species on the N-doped graphitic carbon can be considered negligible.

Similarly to the case of FeP/NG, the high-resolution Ni 2p3/2 spectrum of the NiP/NG sample shows two components coupled at 853.6/860.5 and 856.6/863.2 eV, attributable to $Ni^{\delta+}$ (in Ni_2P) and oxidized Ni species, together with the corresponding satellites.[29] Similarly to Fe_2P, the binding energy values for Ni in Ni_2P are +0.6 eV shifted from the reported values, also indicating an strong interaction between them. The P 2p spectrum of NiP/NG shows two peaks at 129.9 and 133.1 eV attributed also to P 2p3/2 and P 2p1/2 of metal phosphides ($P^{\delta-}$) and P-C, respectively.

The high-resolution XPS C1s, N1s, and O1s spectra of NG, FeP/NG, and NiP/NG are shown in Figure S3 in the supplementary information. As can be seen there, the graphitic support suffered negligible changes upon metal phosphides grafting. The C 1s spectra show four components at 284.5, 285.3, 286.2, and 288.9 eV assigned to sp^2 C, C-N, C-O, and O=C-O, respectively, in all samples. However, it is worth noticing than the component at 285.3 eV, assigned to C-N bonds in NG, has a larger contribution in FeP/CN (27%) and NiP/NG (25%) than that of NG (17%). It has been previously reported that C-P bonds also present a peak centered at 285.3 eV,[24] so this peak in FeP/NG and NiP/NG could be the combination of C-N and C-P components. This can also be taken as evidence of the strong interaction between the graphenic support and the metal phosphides. The N 1s spectra show three components 398.0, 400.5, and 403.5 eV that can be ascribed to pyridinic-N, graphenic-N, and N-oxides, respectively. Finally, O 1s spectra show two components related to C-O and O=C-O bonds in all samples. It is worth noticing that additional components in FeP/NG and NiP/NG, related to the P-O bond, have been determined.

This XPS analysis is in good agreement with the XRD and ICP-OES data, thus confirming that pure Fe_2P, FeP, and Ni_2P are present in FeP/NG and NiP/NG samples, respectively, and additionally, the obtained data point out a strong interaction between the metal phosphides and the graphitic support.

In view of these results, the following reaction mechanism for metal phosphides formation on the N-doped graphene support is proposed. First, it has been widely reported that the pyrolysis of carbon precursors results in the chemical reduction of transition metals and phosphate to elemental phosphorous.[30–32] Then, it has been also reported that phosphorous oxide (P_4O_{10}) can react with carbon under inert atmosphere and be converted into red phosphorous.[33] Thus, simultaneous reduction of metal ions to metal nanoparticles and phosphorous oxide to elemental phosphorous taking place during pyrolysis and the high temperatures will favor their reaction, forming the metal phosphides. Actually, it is reported that metallic Ni can be directly phosphorized to Ni_2P even at temperatures as low as 200°C in the presence of red phosphorous,[14] while FeP has been easily obtained from milling of Fe and red phosphorous.[34] The proposed mechanism is illustrated in Scheme 1.

The metal phosphides and support morphology were studied by HRFESEM and high-resolution transmission electron microscopy (HRTEM). HRFESEM images of FeP/NG, NiP/NG, and NG samples show very similar spongy coral-like morphology, indicating that the supported metal phosphides have not altered the N-doped graphitic carbon structure (see Figure S4 in supplementary information). HRTEM images (Figure 2) allowed to measure 0.20, 0.22, and 0.20 nm lattice fringes, corresponding to the interplanar distance of the (201) facet of Fe_2P, and (111) and (201) facets and Ni_2P, respectively.[35–37] The selected area electron diffraction (SAED) pattern of Fe_2P and Ni_2P is displayed also in Figure 2. The metal phosphides nanoparticles present a round-like morphology. HRTEM images show Ni_2P nanoparticles

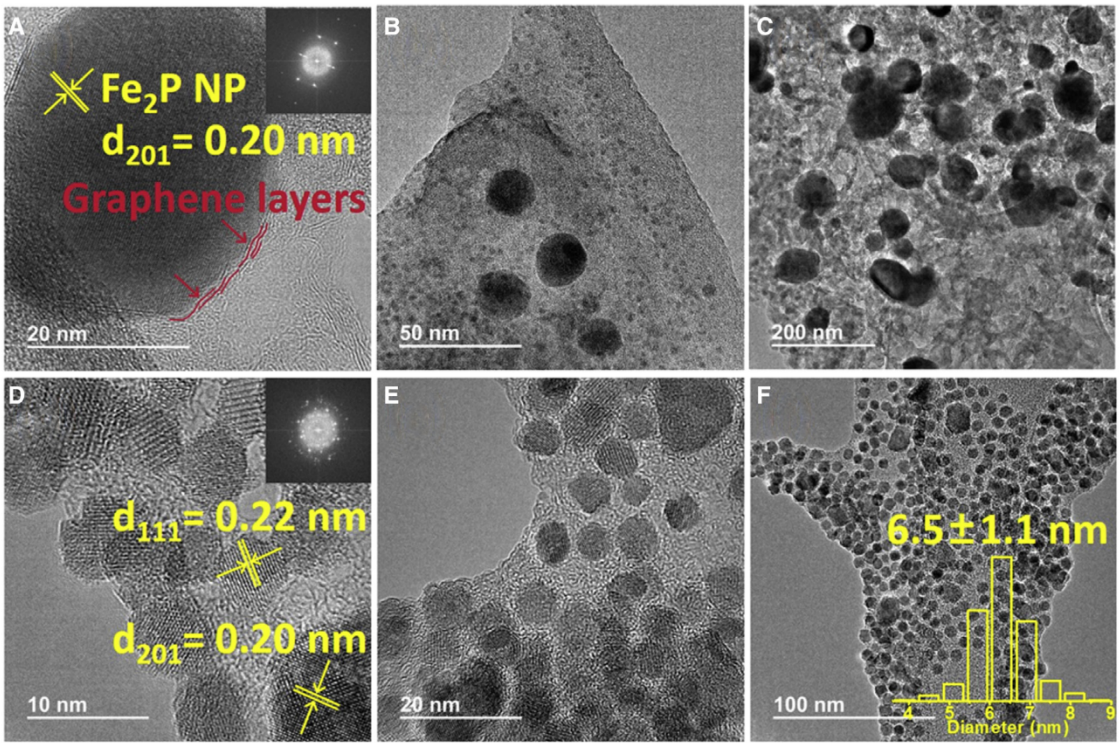

Figure 2. Microscopy characterization of the FeP/NG and NiP/NG samples

HRTEM images of FeP/NG (A–C) and NiP/NG (D–F). SAED patterns of Fe_2P and Ni_2P are included as insets in (A) and (D), respectively. The lattice fringes of the (201) facet in Fe_2P and the (111) and (201) planes of Ni_2P are indicated in (A) and (D), respectively. The histogram of Ni_2P particle size distribution is included in (F).

homogeneously distributed with an average diameter of 6.5 $\pm$ 1.1 nm, after measurement of a statistically relevant number of samples. However, Fe_2P and FeP nanoparticles present a much wider size distribution, ranging from 20 to 200 nm, approximately. Energy-dispersive X-ray spectroscopy and elemental mapping of representative FeP/NG and NiP/NG scanning transmission electron microscopy (STEM) images (Figures S5 and S6 in supplementary information) confirm that the nanoparticles supported on the graphitic matrix are constituted of Fe and P or Ni and P, in Fe_xP/NG and NiP/NG samples, respectively.

The textural properties of FeP/NG, NiP/NG, and NG samples were measured by isothermal nitrogen adsorption/desorption measurements, and the results are also included in Table 1. FeP/NG, NiP/NG, and NG exhibit a Brunauer-Emmett-Teller (BET) surface area of 249, 401, and 272 m^2/g, respectively. Additionally, cyclic voltammetry of all samples at different scan rates in 1 M KOH allowed us to determine the electrochemical active surface area (ECSA) by measuring double-layer capacitance (C_{DL}). As shown in Figure S7 in the supplementary information, FeP/NG and NiP/NG presented very similar C_{DL}, 3.06 and 2.72 mF cm^{-2}, respectively, but higher than that of NG (1.10 mF cm^{-2}), suggesting that metal phosphides present similar amounts of electrocatalytic active sites.

Hydrogen evolution reaction

The electrocatalytic activity of FeP/NG and NiP/NG catalysts for HER was investigated in a 1 M KOH solution by using a three-electrode cell. For comparison purposes, benchmark Pt/C electrocatalyst was also employed for the HER under

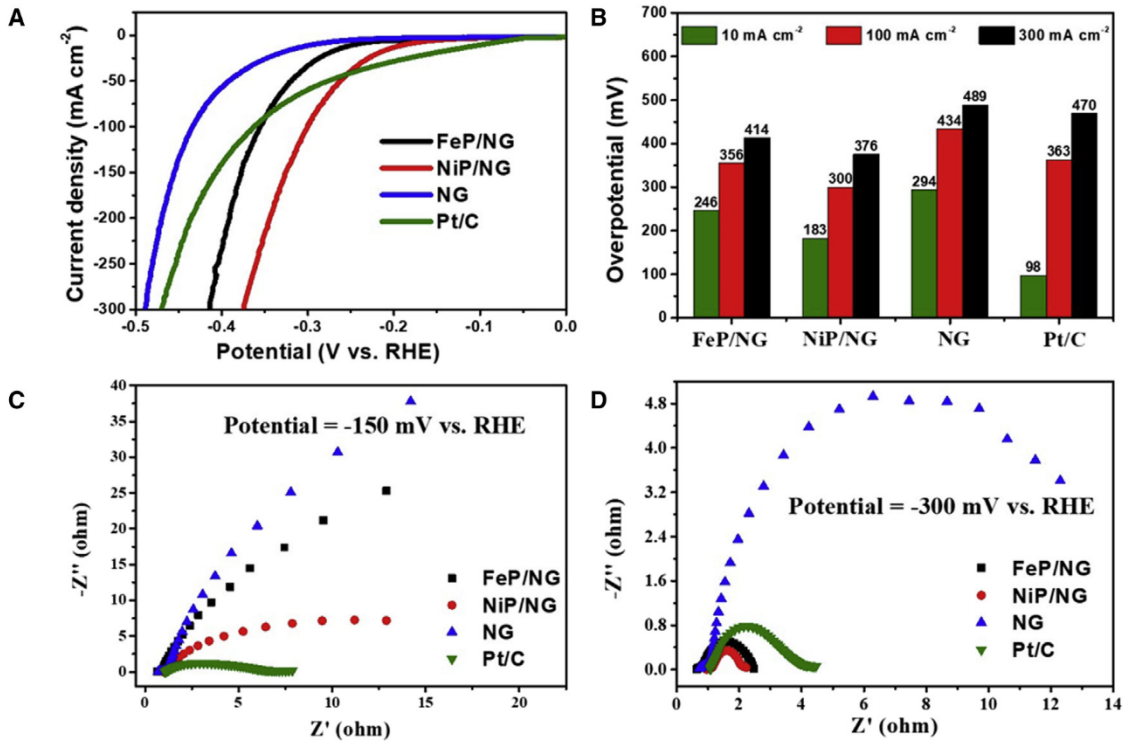

Figure 3. HER performance of FeP/NG, NiP/NG, NG, and Pt/C

(A) Linear scanning voltammetry (LSV) curves showing the crossing of Pt/C plot through the NiP/NG and FeP/NG lines, (B) comparison of the overpotential of the different samples at 10, 100, and 300 mA/cm^2, and Nyquist plots at −150 mV versus RHE (C) and −300 mV versus RHE (D).

identical conditions. As can be seen in Figures 3A and 3B, the Pt/C-based electrode showed the best catalytic activity at 10 mA/cm^2, with an overpotential for HER of 98 mV, while the overpotentials, at same current density, measured for FeP/NG and NiP/NG were 246 and 183 mV, respectively. Remarkably, NiP/NG electrode showed lower overpotentials (300 and 376 mV) than that of Pt/C (363 and 470 mV) at 100 and 300 mA/cm^2, respectively, while the overpotentials of FeP/NG at these current densities were of 356 and 414 mV, respectively. Hence, NiP/NG showed better electrocatalytic activity for HER than FeP/NG in alkali electrolyte. For comparison purposes, the ECSA normalized current from these samples for HER is presented in Figure S8 in the supplementary information, obtaining an identical trend.

The improved catalytic activity of NiP/NG is evidenced in the Tafel plot (Figure S9A in the supplementary information). As it can be observed there, the Tafel slope of NiP/NG (68.9 mV dec^{-1}) was lower than that of FeP/NG (128.2 mV/dec^{-1}), indicating faster reaction kinetics in NiP/NG, explaining its higher HER efficiency. Notably, the Tafel slope for the commercial Pt/C (88.6 mV dec^{-1}) was also higher than that of NiP/NG.

The measured Tafel slope values have also been used to study the most probable HER mechanism. It is well known that HER mechanism in alkaline medium can follow Volmer-Heyrovsky or Volmer-Tafel paths, as shown in Equations 3–5.[38] In the present case, NiP/NG Tafel slope indicates the occurrence of a Volmer-Heyrovsky mechanism. This mechanism is also common for Pt/C and FeP/NG, while the high FeP/NG Tafel slope value suggests the Volmer step (Equation 3) as the limiting step.

$$H_2O + e^- \rightarrow H^* + HO^- \text{ Volmer step} \quad \text{(Equation 3)}$$

$$H_2O + e^- + H^* \rightarrow H_2 + HO^- \text{ Heyrovsky step} \quad \text{(Equation 4)}$$

$$H^* + H^* \rightarrow H_2 \text{ Tafel step} \quad \text{(Equation 5)}$$

In order to further investigate the charge transfer kinetics in these electrodes under alkaline conditions, electrochemical impedance spectroscopy (EIS) of all samples at different potentials was measured. The Nyquist plots (Figures 3C and 3D) of NiP/NG exhibited a larger semicircle at −150 mV versus RHE than that of Pt/C, indicating slower charge transfer at this overpotential. However, the charge transfer resistance at larger potential (−300 mV versus RHE), corresponding to a current density of 100 mA/cm^2, approximately, for NiP/NG was lower than that of Pt/C. The experimental data obtained from Nyquist plots was fitted to a simple equivalent circuit model, and the obtained parameters and the equivalent circuit are presented in Table S1 in the supplementary information. From these data, it can be observed that the obtained charge transfer resistance (R_{CT}) of NiP/NG is significantly lower than that of FeP/NG. Moreover, the R_{CT} in NiP/NG at −150 mV is much higher (15.4 Ω/cm^2) than that of the commercial Pt/C (2.2 Ω/cm^2), while at −300 mV the R_{CT} in NiP/NG is 3-fold lower than that of Pt/C. This change in the relative order of the charge transfer resistance for NiP/NG and Pt/C is in accordance with the measurements corresponding to the Nyquist plot.

Oxygen evolution reaction

Besides a remarkable catalytic activity for HER in alkali conditions, specially at high current densities, FeP/NG and NiP/NG have also demonstrated excellent OER performance in 1 M KOH electrolyte, as shown in Figures 4A and 4B. In this case, FeP/NG electrocatalysts exhibit lower overpotential (217 mV) than NiP/NG (264 mV) at 10 mA cm^{-2} for OER. Benchmark RuO_2 electrodes were tested for comparison purposes, and the observed overpotential at this current density was 183 mV, lower than those of the metal phosphides on N-doped graphene. Interestingly, at larger current density, near commercial requirements (300 mA cm^{-2}), FeP/NG has demonstrated to be more efficient than the commercial RuO_2 electrocatalysts, exhibiting overpotential of 292 mV at 300 mA cm^{-2}, while the overpotential with the commercial RuO_2 electrode was 308 mV at the same current density. For comparison purposes, the ECSA normalized current from these samples for OER is presented in Figure S10 in the supplementary information, obtaining an identical trend.

Furthermore, the excellent catalytic activity for OER of FeP/NG electrocatalyst was also corroborated from the Tafel plot (Figure S9B). FeP/NG showed a Tafel slope of 30.5 mV dec^{-1}, which is significantly lower than that of NiP/NG (53.2 mV dec^{-1}) and RuO_2 (55.4 mV dec^{-1}), suggesting faster OER kinetics.

The OER mechanism under alkaline conditions is a four electron process, following Equations 6–10.

$$M + OH^- \rightleftarrows MOH + e^- \text{ Step 1} \quad \text{(Equation 6)}$$

$$MOH + OH^- \rightleftarrows MO + H_2O + e^- \text{ Step 2} \quad \text{(Equation 7)}$$

$$MO + OH^- \rightleftarrows MOOH + e^- \text{ Step 3} \quad \text{(Equation 8)}$$

$$MOOH + OH^- \rightleftarrows MOO^- + H_2O \text{ Step 4} \quad \text{(Equation 9)}$$

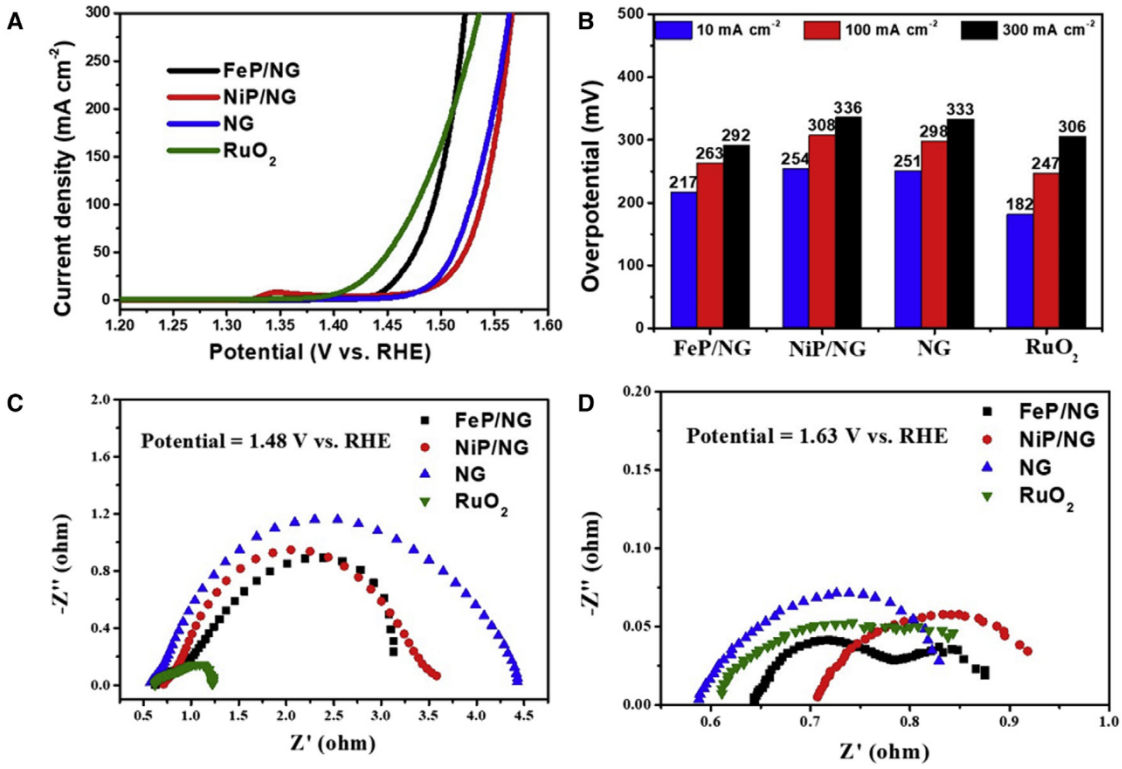

Figure 4. OER performance of FeP/NG, NiP/NG, NG, and RuO_2

(A) LSV curves showing the crossing of the RuO_2 line with the FeP/NG plot, (B) comparison of the overpotential of the different samples at 10, 100, and 300 mA/cm^2, and Nyquist plots at 1.48 versus RHE (C) and 1.63 mV versus RHE (D).

$$MOO^- \rightleftarrows M + O_2 + e^- \text{ Step 5} \qquad \text{(Equation 10)}$$

The low FeP/NG Tafel slope (30.5 mV dec^{-1}) indicates that the second step (Equation 7), when surface-adsorbed species produced in the early stage of the OER remain predominant, determines the overall rate.[39] However, the higher NiP/NG and RuO_2 Tafel slopes may suggest the formation of O, OOH, or OO intermediates (Equations 8–10) as the rate limiting steps, with step 3 (OOH) being the most probable.[40]

Additionally, the charge transfer reactions were investigated for all catalysts by EIS, and the results are presented in Figures 4C and 4D. According to these, RuO_2 electrodes exhibited the lowest resistance to charge transfer at 1.48 V versus RHE, corresponding approximately to 10 mA/cm^2. However, at larger potential (1.63 V versus RHE), FeP/NG has demonstrated the fastest charge transfer kinetics. The experimental data has been fitted to an equivalent circuit, and the obtained parameters are summarized in Table S2 in the supplementary information.

Water electrolysis

Inspired by the aforementioned HER and OER remarkable performance at high current densities of NiP/NG and FeP/NG, water electrolysis in alkaline solution was performed by operating a two-electrode configuration using NiP/NG and FeP/NG as cathode and anode, respectively, for 150 h. For comparison purposes, an analogous two-electrode cell constructed with benchmark Pt/C and RuO_2 catalysts, as cathode and anode, respectively, was also prepared, and its performance for overall water

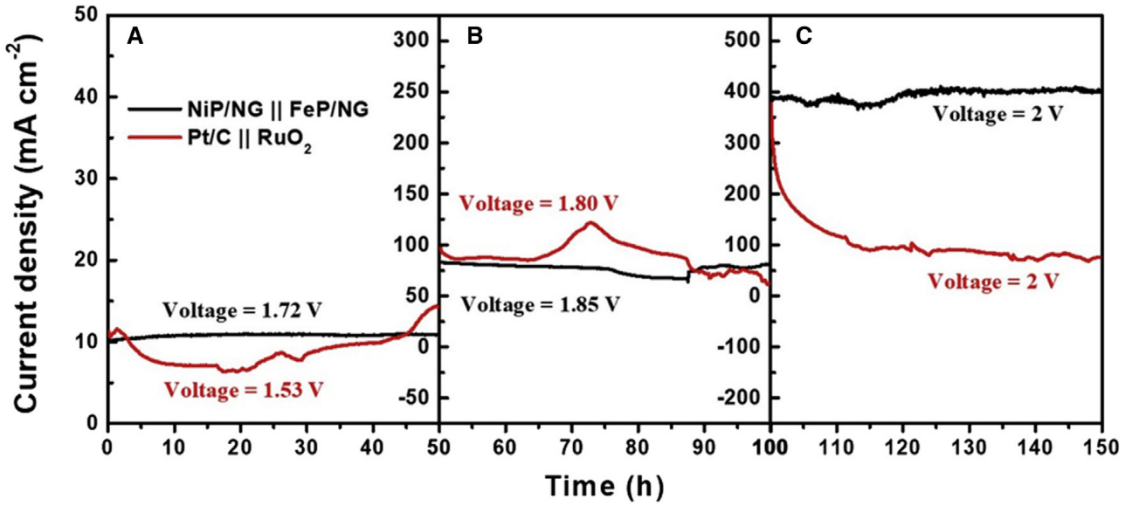

Figure 5. Water electrolysis at different potential for 150 h

Chronoamperometry of commercial Pt/C-RuO_2 (red) and NiP/NG-FeP/NG cell (black) for continuous 150 h with increasing the applied voltage at 1.7 V and 1.5 V for NiP/Ng-FeP/NG and Pt/C-RuO2, respectively (A), 1.8 V (B) and 2 V (C) every 50 h.

splitting was determined. As observed in Figure 5A, NiP/NG-FeP/NG cell achieved 10 mA/cm^2, approximately, applying 1.72 V constantly for 50 h. However, only 1.53 V was needed to obtain similar current density with the Pt/C-RuO_2 cell in the same period. After 50 h, the cell voltages were increased to 1.8 and 1.85 V for the commercial Pt/C-RuO_2 and NiP/NG-FeP/NG electrodes, respectively, and maintained for an additional 50 h (Figure 5B). In this case, current densities near 100 mA/cm^2 were obtained in both cells. Finally, 2 V was applied in both cells for another 50 h, accounting for a stability test of 150 h in total (Figure 5C). At 2 V, it can be clearly observed that initial current density of 400 mA/cm^2 was obtained in both cells. However, the commercial Pt/C-RuO_2 cell immediately suffered a current density drop down to 100 mA/cm^2, approximately, while the NiP/NG-FeP/NG electrode kept the current density constant for the 50 h test.

These results clearly indicate that the benchmark Pt/C-RuO_2 electrodes are more efficient than that of the NiP/NG-FeP/NG electrodes for the overall water splitting reaction in alkali conditions at low current densities (10 mA/cm^2). At moderate current density (100 mA/cm^2), both the commercial Pt/C-RuO_2 and the NiP/NG-FeP/NG electrodes perform similarly. Importantly, at high current density in the range used in commercial applications (400 mA/cm^2), the NiP/NG-FeP/NG electrodes perform much better than the commercial ones.

Nyquist plots measured in the NiP/NG-FeP/NG and Pt/C-RuO_2 cells at 1.7 and 2 V are presented in Figure S11 in the supplementary information, and the parameters obtained from the experimental data fitting to an equivalent circuit are summarized in Table S3. As can be seen there, the charge transfer resistance in NiP/NG-FeP/NG at 1.7 V is larger than that of Pt/C-RuO_2. However, Pt/C-RuO_2 presents a 3.6-fold increase in charge transfer resistance at 2 V, while NiP/NG-FeP/NG's charge transfer resistance decreases 6.8-fold. It is worth commenting that FeP/NG-NiP/NG catalysts outperform most of the reported metal phosphides supported on carbon-based materials, especially at high current densities, near the commercial requirements (see Table S4 in the supplementary information). This improved performance derives from the preparation procedure in which both N-doped graphene and metal

phosphide nanoparticles are formed simultaneously at high temperature (900°C), establishing a strong interaction without interference of solvent molecules or ligands.

Moreover, NiP/NG-FeP/NG electrodes have demonstrated better stability than the reference Pt/C-RuO_2 electrodes, as can be seen in Figure 5, especially at large current density. Evidence of this stability is provided by representative STEM images presented in Figure S12 in the supplementary information of NiP/NG and FeP/NG materials as prepared and after the 150 h chronoamperometry at increasing applied bias. As can be seen there, shape and size of the metal phosphide nanoparticles did not suffer significant changes upon this long-term test, demonstrating its stability. Moreover, the nanoparticle crystallinity also remained unaltered after this electrocatalytic reaction, as can be observed in the HRTEM images presented in Figure S13. In these images, the SAED pattern and the measurements of 0.27, 0.20, and 0.22 nm lattice fringes, corresponding to interplanar distances of the (001), (201), and (111) facets of FeP, Fe_2P, and NiP, respectively, confirm their high crystallinity under these reaction conditions.

The present manuscript describes a potentially green and sustainable procedure for the preparation of Ni and Fe phosphides grafted on N-doped graphene that avoids the use or generation of extremely hazardous PH_3. This new methodology enhances the interaction between the electrically conductive graphene and the metal phosphide resulting in improved HER and OER electrodes. These metal phosphides on graphene outperform in terms of required overpotential and stability the performance of benchmark electrodes made of Pt or Ru for high current densities required in commercial water electrolysis. The present procedure may open the door also for the preparation of bi- and multimetallic phosphides supported on various graphenes to develop a new generation of HER and OER electrodes with advanced performance.

EXPERIMENTAL PROCEDURES

Resource availability

Lead contact

Further information and requests for resources should be directed to and will be fulfilled by the lead contact, Hermenegildo García (hgarcia@qim.upv.es).

Materials availability

This study did not generate new unique reagents.

Data and code availability

The data that support the findings of this study are available from the corresponding authors.

FeP/NG, NiP/NG, and NG preparation procedure

Commercially available reagents were purchased from Aldrich and used without further purification.

Briefly, 1,000 mg chitosan, 625 μL acetic acid, and 3 mmol $Fe(OAc)_2$ or $Ni(OAc)_2{\cdot}4H_2O$ were added into 50 mL milli-Q water. After chitosan dissolved completely, the solution was introduced drop-wise, with a syringe (0.8-mm diameter needle) in an aqueous solution of sodium hydroxide (2 M, 500 mL). The gel microspheres were formed and immersed in NaOH solution for 2h, then profusely washed with distilled water to pH = 7. Then the resulting hydrogel microspheres were washed by a series of ethanol/water baths with an increasing concentration of

ethanol (10, 30, 50, 70, 90, and 100 vol %, respectively) for 15 min in each. After that, the microspheres were impregnated in 100 mL P_4O_{10}-ethanol solution (9 mM) for 2 days and exchanged by supercritical CO_2. The resulting microspheres were pyrolyzed under Ar flow (200 mL/min), increasing the temperature at a rate of 2°C/min up to 200°C for 2h and then to 900°C for 2 h. Sample NG was prepared without the addition of metal salts.

Sample characterization

HRFESEM images were acquired by using a ZEISS GeminiSEM 500 apparatus. HRTEM images were recorded in a JEOL JEM 2100F under an accelerating voltage of 200 kV. Samples were prepared by applying one drop of the suspended material in ethanol onto a carbon-coated copper TEM grid and allowing them to dry at room temperature. Raman spectra were collected with a Horiba Jobin Yvon-Labram HR UV-visible-NIR (200–1,600 nm) Raman Microscope Spectrometer using a 514-nm laser. The chemical composition of the samples was determined by combustion chemical analysis by using a CHNS FISONS elemental analyzer. XPS were measured on an SPECS spectrometer equipped with a Phoibos 150 MCD-9 detector using a non-monochromatic X-ray source (Al) operating at 200 W. Before spectrum collection, samples were evacuated in the prechamber of the spectrometer at 1×10^{-9} mbar. The measured intensity ratios of the components were obtained from the area of the corresponding peaks after nonlinear Shirley-type background subtraction and corrected by the transition function of the spectrometer.

Electrochemical characterization

The working electrode was prepared using a mixture of the active catalyst, carbon black, and polyvinylidene fluoride (PVDF) as binder in 8:1:1 ratio. This mixture was ground in mortar using N-methyl-2-pyrrolidone (NMP) and ethanol as solvents. This slurry was brushed onto one side of nickel foam, and then it was folded in half. After drying overnight at 60°C, the foam was pressed at 10 MPa for 60 s.

In the electrochemical measurement, the as-fabricated electrode, Hg/HgO electrode, and a carbon rod were used as the working electrode, reference electrode, and counter-electrode, respectively. The 1 M KOH was used as electrolyte. iR compensation was conducted for all curves (see Figure S13).

The OER, HER, and overall water splitting activities were assessed by linear sweep voltammetry (LSV) under a small sweep speed (1 mV/s) in 1 M KOH. Double-layer capacitance of catalysts was determined from cyclic voltammetry curves with sweep rates from 10 to 50 mV/s. The EIS of samples was conducted at different overpotential with a frequency range of 0.01Hz–100 kHz. The calibration of the Hg/HgO reference electrode was carried out in a three-electrode electrolytic cell. Two Pt electrodes were used as the working electrode and the counter electrode, with the Hg/HgO electrode as the reference electrode. H_2 was bubbled into the 1 M KOH electrolyte in the electrochemical cell until it was saturated, and then the LSV was conducted (see Figure S11).

SUPPLEMENTAL INFORMATION

Supplemental information can be found online at https://doi.org/10.1016/j.xcrp.2022.100873.

ACKNOWLEDGMENTS

Financial support by the "MCIN/AEI/10.13039/501100011033/ y por FEDER Una manera de hacer Europa" (RTI2018-098237-B-C21) and Generalitat Valenciana

(Prometeo 2021-038) are gratefully acknowledged. The European Union project H2020-LC-SC3-2020-RES-RIA "EcoFuel"(grant agreement 101006701) is also gratefully acknowledged. J.H. thanks the Chinese Scholarship Council for doctoral fellowship. L.P. also thanks the Generalitat Valenciana for a Grisolia postgraduate scholarship.

AUTHOR CONTRIBUTIONS

J.H. and L.P. contributed equally in the materials preparation, characterization, and electrochemical tests. A.P. supervised the materials preparation and characterization. The work was supervised by J.A. and H.G., who wrote the draft. The manuscript was revised by all the authors.

DECLARATION OF INTERESTS

The authors declare no competing interests.

Received: December 15, 2021
Revised: January 28, 2022
Accepted: April 7, 2022
Published: April 28, 2022

REFERENCES

1. Hydrogen on the rise, Nat. Energy, 1 (2016), pp. 16127.
2. Hacker, V., and Mitsushima, S. (2018). Fuel Cells and Hydrogen: From Fundamentals to Applied Research (Elsevier Science).
3. Abdin, Z., Zafaranloo, A., Rafiee, A., Mérida, W., Lipiński, W., and Khalilpour, K.R. (2020). Hydrogen as an energy vector. Renew. Sustain. Energy Rev. *120*, 109620.
4. Jiao, Y., Zheng, Y., Jaroniec, M., and Qiao, S.Z. (2015). Design of electrocatalysts for oxygen- and hydrogen-involving energy conversion reactions. Chem. Soc. Rev. *44*, 2060–2086.
5. Mallouk, T.E. (2013). Divide and conquer. Nat. Chem. *5*, 362–363.
6. You, B., and Sun, Y. (2018). Innovative strategies for electrocatalytic water splitting. Acc. Chem. Res. *51*, 1571–1580.
7. Grigoriev, S.A., Fateev, V.N., Bessarabov, D.G., and Millet, P. (2020). Current status, research trends, and challenges in water electrolysis science and technology. Int. J. Hydrogen Energy *45*, 26036–26058.
8. Roger, I., Shipman, M.A., and Symes, M.D. (2017). Earth-abundant catalysts for electrochemical and photoelectrochemical water splitting. Nat. Rev. Chem. *1*, 0003.
9. Zhu, Y.P., Guo, C., Zheng, Y., and Qiao, S.-Z. (2017). Surface and interface engineering of noble-metal-free electrocatalysts for efficient energy conversion processes. Acc. Chem. Res. *50*, 915–923.
10. Zou, X., and Zhang, Y. (2015). Noble metal-free hydrogen evolution catalysts for water splitting. Chem. Soc. Rev. *44*, 5148–5180.
11. Kim, B., Kim, T., Lee, K., and Li, J. (2020). Recent advances in transition metal phosphide electrocatalysts for water splitting under neutral pH conditions. ChemElectroChem *7*, 3578–3589.
12. Wang, Y., Kong, B., Zhao, D., Wang, H., and Selomulya, C. (2017). Strategies for developing transition metal phosphides as heterogeneous electrocatalysts for water splitting. Nano Today *15*, 26–55.
13. Wang, X., Kolen'ko, Y.V., Bao, X.-Q., Kovnir, K., and Liu, L. (2015). One-step synthesis of self-supported nickel phosphide nanosheet array cathodes for efficient electrocatalytic hydrogen generation. Angew. Chem. Int. Ed. *54*, 8188–8192.
14. Wang, X., Kolen'ko, Y.V., and Liu, L. (2015). Direct solvothermal phosphorization of nickel foam to fabricate integrated Ni2P-nanorods/Ni electrodes for efficient electrocatalytic hydrogen evolution. Chem. Commun. *51*, 6738–6741.
15. Ali, A., and Shen, P.K. (2020). Nonprecious metal's graphene-supported electrocatalysts for hydrogen evolution reaction: fundamentals to applications. Carbon Energy *2*, 99–121.
16. Shams, S.S., Zhang, L.S., Hu, R., Zhang, R., and Zhu, J. (2015). Synthesis of graphene from biomass: a green chemistry approach. Mater. Lett. *161*, 476–479.
17. Zhao, X., Fan, Y., Wang, H., Gao, C., Liu, Z., Li, B., Peng, Z., Yang, J.-H., and Liu, B. (2020). Cobalt phosphide-embedded reduced graphene oxide as a bifunctional catalyst for overall water splitting. ACS Omega *5*, 6516–6522.
18. Zhang, H., Maijenburg, A.W., Li, X., Schweizer, S.L., and Wehrspohn, R.B. (2020). Bifunctional heterostructured transition metal phosphides for efficient electrochemical water splitting. Adv. Funct. Mater. *30*, 2003261.
19. Han, Y., Chen, Y., Fan, R., Li, Z., and Zou, Z. (2021). Promotion effect of metal phosphides towards electrocatalytic and photocatalytic water splitting. EcoMat *3*, e12097.
20. Primo, A., and Quignard, F. (2010). Chitosan as efficient porous support for dispersion of highly active gold nanoparticles: design of hybrid catalyst for carbon–carbon bond formation. Chem. Commun. *46*, 5593–5595.
21. Primo, A., Forneli, A., Corma, A., and García, H. (2012). From biomass wastes to highly efficient CO2 adsorbents: graphitisation of chitosan and alginate biopolymers. ChemSusChem *5*, 2207–2214.
22. Mateo, D., Esteve-Adell, I., Albero, J., Royo, J.F.S., Primo, A., and Garcia, H. (2016). 111 oriented gold nanoplatelets on multilayer graphene as visible light photocatalyst for overall water splitting. Nat. Commun. *7*, 11819.
23. Primo, A., Atienzar, P., Sanchez, E., Delgado, J.M., and García, H. (2012). From biomass wastes to large-area, high-quality, N-doped graphene: catalyst-free carbonization of chitosan coatings on arbitrary substrates. Chem. Commun. *48*, 9254–9256.
24. Yao, Y., Mahmood, N., Pan, L., Shen, G., Zhang, R., Gao, R., Aleem, F.-e., Yuan, X., Zhang, X., and Zou, J.-J. (2018). Iron phosphide encapsulated in P-doped graphitic carbon as efficient and stable electrocatalyst for hydrogen and oxygen evolution reactions. Nanoscale *10*, 21327–21334.
25. Ma, F.-X., Xu, C.-Y., Lyu, F., Song, B., Sun, S.-C., Li, Y.Y., Lu, J., and Zhen, L. (2019). Construction of FeP hollow nanoparticles densely encapsulated in carbon nanosheet frameworks for efficient and durable electrocatalytic hydrogen production. Adv. Sci. *6*, 1801490.
26. Mateo, D., Albero, J., and García, H. (2018). Graphene supported NiO/Ni nanoparticles as efficient photocatalyst for gas phase CO2

reduction with hydrogen. Appl. Catal. B: Environ. *224*, 563–571.

27. Tang, K., Wang, X., Wang, M., Xie, Y., Zhou, J., and Yan, C. (2017). Ni/Fe ratio dependence of catalytic activity in monodisperse ternary nickel iron phosphide for efficient water oxidation. ChemElectroChem *4*, 2150–2157.

28. Zong, W., Chui, N., Tian, Z., Li, Y., Yang, C., Rao, D., Wang, W., Huang, J., Wang, J., Lai, F., and Liu, T. (2021). Ultrafine MoP nanoparticle splotched nitrogen-doped carbon nanosheets enabling high-performance 3D-printed potassium-ion hybrid capacitors. Adv. Sci. *8*, 2004142.

29. Gao, R., Pan, L., Wang, H., Zhang, X., Wang, L., and Zou, J.-J. (2018). Ultradispersed nickel phosphide on phosphorus-doped carbon with tailored d-band center for efficient and chemoselective hydrogenation of nitroarenes. ACS Catal. *8*, 8420–8429.

30. He, J., Dhakshinamoorthy, A., Primo, A., and Garcia, H. (2017). Iron nanoparticles embedded in graphitic carbon matrix as heterogeneous catalysts for the oxidative C−N coupling of aromatic N−H compounds and amides. ChemCatChem *9*, 3003–3012.

31. Ma, Z., Tsounis, C., Kumar, P.V., Han, Z., Wong, R.J., Toe, C.Y., Zhou, S., Bedford, N.M., Thomsen, L., Ng, Y.H., and Amal, R. (2020). Enhanced electrochemical CO2 reduction of Cu@CuxO nanoparticles decorated on 3D vertical graphene with intrinsic sp3-type defect. Adv. Funct. Mater. *30*, 1910118.

32. Abellán, G., Latorre-Sánchez, M., Fornés, V., Ribera, A., and García, H. (2012). Graphene as a carbon source effects the nanometallurgy of nickel in Ni,Mn layered double hydroxide–graphene oxide composites. Chem. Commun. *48*, 11416–11418.

33. Hocking, M.B. (2006). Handbook of Chemical Technology and Pollution Control, 3rd Edition (Elsevier Inc.).

34. Li, W., Yan, B., Fan, H., Zhang, C., Xu, H., Cheng, X., Li, Z., Jia, G., An, S., and Qiu, X. (2019). FeP/C composites as an anode material for K-ion batteries. ACS Appl. Mater. Inter. *11*, 22364–22370.

35. Liang, B., Hu, X., Sun, D., Yang, Q., Tang, H., Zuo, X., Lin, Y., and Li, G. (2021). Facile fabrication of bimetallic Fe2P–Ni2P heterostructure for boosted oxygen evolution. J. Mater. Sci. Mater. Electronics *32*, 23420–23428.

36. Cao, S., Chen, Y., Wang, C.-J., He, P., and Fu, W.-F. (2014). Highly efficient photocatalytic hydrogen evolution by nickel phosphide nanoparticles from aqueous solution. Chem. Commun. *50*, 10427–10429.

37. Wang, M., Lin, M., Li, J., Huang, L., Zhuang, Z., Lin, C., Zhou, L., and Mai, L. (2017). Metal–organic framework derived carbon-confined Ni2P nanocrystals supported on graphene for an efficient oxygen evolution reaction. Chem. Commun. *53*, 8372–8375.

38. Mahmood, N., Yao, Y., Zhang, J.-W., Pan, L., Zhang, X., and Zou, J.-J. (2018). Electrocatalysts for hydrogen evolution in alkaline electrolytes: mechanisms, challenges, and prospective solutions. Adv. Sci. *5*, 1700464.

39. Shinagawa, T., Garcia-Esparza, A.T., and Takanabe, K. (2015). Insight on Tafel slopes from a microkinetic analysis of aqueous electrocatalysis for energy conversion. Scientific Rep. *5*, 13801.

40. Alobaid, A., Wang, C., and Adomaitis, R.A. (2018). Mechanism and kinetics of HER and OER on NiFe LDH films in an alkaline electrolyte. J. Electrochem. Soc. *165*, J3395–J3404.